

# Development of Unconventional Nano-Metamaterials from Viral Nano-Building Blocks

Paolo Passaretti, Zoe Schofield, Jonathan James Stanley Rickard, Henry White, Sumeet Mahajan, and Pola Goldberg Oppenheimer\*

Structured metamaterials are periodically arranged nanostructures in which the dielectric constant is periodically modulated on a length-scale comparable to the desired wavelength of operation. Interactions of the electric fields of light waves with the sub-wavelength unit structures can produce effects that are impossible in natural materials. Here, a technique to construct three-dimensional (3D) metamaterials using self-assembling M13 viral building-blocks as templates which are then replicated into a metal quasi-3D nanostructure is developed. By correct fit of virus fragments, it is possible to employ them in a LEGO-like way to build up well-defined structures on the nanoscale. The virus blocks are designed to spontaneously assemble into 3D-periodic network structures with interesting optical properties. Subsequently, templating of these nanostructures into inorganic materials allows the replication of their network into an inverse periodic metal structure, which has the appropriate architecture for optical metamaterials. Establishing such a technique provides an important link toward the realization of applied metamaterials potentially heralding a new era for developing novel types of bio-synthetic optical materials. These materials have a wide range of potential uses including cloaking materials, light-storage devices, high-speed optical computers and nano-lasers, and will offer numerous applications in transformation optics.

example is the invisibility cloak, just like in the Harry Potter movies. Once it is slipped over something, it makes the object vanish. A possible real-world implementation of this “magical” garment is based on optical *metamaterials*, which are periodic structures at the nanoscale. Correctly designed nanostructures can guide light waves around an object, reminiscent of a rock diverting water in a stream, and effectively making it invisible. Additionally, nanostructures with periodicities that are comparable to the light wavelength, typically 200–1000 nm, i.e., photonic bandgap (PBG) materials, can trap certain colors of light. On the other hand, photonic metamaterials are based on the periodically arranged structures on the sub-100-nm length scale, which have the capability to modulate electromagnetic waves in an unusual fashion and are predicted to produce super-lenses, stealth or cloaking devices.<sup>[1]</sup> PBG metamaterials are another class of dielectric nanostructures which have patterning at the wavelength as well

## 1. Introduction

Exciting scientific developments laying foundations for new technologies will enable us to engineer the properties of materials in ways previously believed impossible. A prominent


as sub-wavelength scale or just the latter but create a photonic band gap as well as result in negative refraction or other unusual effects.<sup>[2]</sup> They have a wavelength band gap in which light propagation is forbidden. Selective trapping and control of light propagation enables engineering the fundamental properties

P. Passaretti, Z. Schofield, P. Goldberg Oppenheimer  
School of Chemical Engineering  
Advanced Nanomaterials Structures and Applications Laboratories  
College of Engineering and Physical Sciences  
University of Birmingham  
Edgbaston, Birmingham B15 2TT, UK  
E-mail: goldberp@bham.ac.uk; p.goldbergoppenheimer@bham.ac.uk

P. Passaretti  
Institute of Cancer and Genomic Sciences  
College of Medical and Dental Sciences  
University of Birmingham  
Edgbaston, Birmingham B15 2TT, UK

Z. Schofield  
School of Life Sciences  
University of Warwick  
Coventry CV4 7AL, UK  
J. J. S. Rickard  
Department of Physics  
Cavendish Laboratory  
University of Cambridge  
JJ Thomson Avenue, Cambridge CB3 0HE, UK  
H. White  
BAE Systems  
Engineering and Sensing  
Buckingham House, Filton, Bristol BS34 7QW, UK

S. Mahajan  
School of Chemistry and the Institute for Life Sciences  
University of Southampton  
Highfield, Southampton SO17 1BJ, UK  
P. Goldberg Oppenheimer  
Healthcare Technologies Institute  
Institute of Translational Medicine  
Mindelsohn Way, Birmingham B15 2TH, UK

 The ORCID identification number(s) for the author(s) of this article can be found under <https://doi.org/10.1002/adom.202102784>.

© 2022 The Authors. Advanced Optical Materials published by Wiley-VCH GmbH. This is an open access article under the terms of the Creative Commons Attribution License, which permits use, distribution and reproduction in any medium, provided the original work is properly cited.

DOI: 10.1002/adom.202102784

(i.e., speed, wavelength, frequency) of electromagnetic waves to produce effects that are impossible with conventional optics. One of the main obstacles to realize these concepts, however, is the enormous difficulty to fabricate periodic three-dimensional (3D) nanostructures to a high level of atomic precision. Making an object vanish in 3D still remains an unachieved challenge. Two-dimensional (2D) optical metamaterials have been widely researched yet, 3D architectures are required to access the exciting full properties of nanostructured metamaterials. The vast majority of earlier approaches to such photonic nano-materials are based on conventional lithographic techniques.<sup>[1b]</sup> These are not only costly and time consuming but are also cumbersome and not scalable. They are intrinsically 2D methods and must be iterated to create a 3D structure. Although stacks consisting of three or four functional layers have been reported, tunable, low-cost and high throughput 3D metamaterials are yet to be developed. The enormous, applied potential of 3D porous nanomaterials has driven extensive research efforts to explore novel processes for the fabrication of highly ordered 3D structures with sub-micrometer periodicities. Several groups have demonstrated the production of sub-micrometer solar-cells and semiconductor arrays using a general templating approach.<sup>[3]</sup> In this approach porous templates were formed via selective degradation of self-assembled phase-separated block copolymer (BCP) morphologies which were further used for patterning of inorganic materials. BCP morphologies which are bicontinuous in all three spatial dimensions are rare and difficult to manufacture.

In contrast, self-assembled viral nanostructures based on the M13 bacteriophage chassis offer a greater versatility. M13 is a filamentous bacteriophage which is 880 nm long by 6.6 nm wide and formed of a protein capsid wrapped around a single stranded circular deoxyribonucleic acid (DNA) genome.<sup>[4]</sup> M13 has been shown to form lyotropic liquid crystal (LC) phases<sup>[5]</sup> and is highly attractive for nanostructuring approach as it is easy to produce (via bacterial fermentation<sup>[6]</sup>), is resistant to disruption by heat<sup>[7]</sup> and solvents<sup>[8]</sup> and yet is easily modified both chemically and genetically to produce particles with different morphologies and chemico-physical characteristics.<sup>[4b,9]</sup> In recent years it has become clear that these nanoarchitectures can be “glued” together via a number of programmed interactions. These nanoarchitectures have been assembled using numerous versions of M13 functionalized ad hoc to interact with other materials via strong covalent bonds<sup>[10]</sup> or other intermolecular interactions.<sup>[11]</sup> In a simplified analogy, modular viral building molecules are similar to LEGO blocks that fit together in a unique way, which can then be used to design complex architectures in terms of both structure and function. Due to these unique properties, M13 bacteriophage has been explored for various functional devices and applications ranging from catalysts to energy harvesting devices, engineering sophisticated functional helical-twisted structures<sup>[12]</sup> and labels in imaging-based diagnosis,<sup>[13]</sup> through photovoltaics,<sup>[14]</sup> and onto biological imaging.<sup>[15]</sup> While M13-based scaffolds have been investigated for directing the assembly of nanoparticles at specific molecular binding sites, for molecular-fuel machines<sup>[16]</sup> and nanostructures for drug delivery,<sup>[17]</sup> the potential for *quasi* 3D viral nanotemplates for the synthesis of inorganic materials still remains mainly untapped.

In this study we harness the inherently precise self-assembly behavior of biomolecules to develop a novel method toward the realization of three-dimensional nano-metamaterials. Our approach is based on viral building blocks that enable the directed assembly of sub-100 nm materials used to fabricate *quasi* 3D nanoarchitectures. This enables the arrangement of nanometric components with characteristic length scales ranging from a few to several hundreds of nanometers and thus, control over variation of dielectric contrast. By exploiting genetically and chemically tunable M13 particles as *bottom-up* building blocks for novel and diverse *quasi* 3D nanostructures, which are unavailable by conventional lithography or polymer chemistry, we exploit the M13 architectures as nano-scaffolds for patterning metals to create novel optical metamaterials and the construction of a new range of nano-network structures of desired morphologies. A range of underlying substrates are fabricated to act as topological cues and guide the M13 self-assembly, yielding vertically aligned and horizontally oriented nanoviral gratings, Fresnel-like nanoarchitectures and chiral LC phase nano-morphologies. Transferring these viral self-assemblies into nanostructured functional material systems is subsequently achieved using a templating approach in which the periodic structure is replicated with metallic materials, such as gold, electrochemically grown from an underlying substrate. Selective degradation of the sacrificial viral template leaves the free-standing *quasi* 3D nanoarchitectures made of gold resulting in a new material, which has the architecture of an optical metamaterial.

Virus-based nanostructuring enables a straightforward and cost-effective formation of nanostructures with two to three characteristic lateral dimensions via the synthetic biology origin to generate lithographically defined architectures. While most micro-to-nano-fabrication techniques utilize resists of macromolecular nature, the extension toward more complex material systems such as viral metamaterials are of major importance for enabling invaluable surface functionalities that cannot be accomplished with resists or polymers alone. Establishing a new *bottom-up* viral nano-assembly structuring technique for developing novel types of materials and properties from biosynthetic biology origin enables a new route of exploiting modified, either genetically and/or chemically M13 particles as *bottom-up* building blocks for novel and diverse nanostructures, which are unavailable by conventional lithography or polymer chemistry. In addition to acting as new free standing nano-morphologies, it is further possible to exploit the assembled bacteriophage nanoarchitectures as scaffolds for further patterning a range of metals, glass or ceramics to create novel properties and optical materials. This could allow the construction of a virtually unlimited range of nano-network structures of any desired morphology. Furthermore, the technique of structuring nanomaterials from viral nano-building blocks is cost-effective, easy to setup and is high throughput with a pattern resolution that can range from nanometer to micrometer precision. Since this method is compatible with aqueous conditions, it is particularly conducive to patterning biomolecules. The lateral size and the height of the nanostructures can be controlled by adjustments of the assembled nanofilm thickness, viral particles concentration, the assembly time and the choice of the guiding substrate.

Although there is a need to utilize another lithography to fabricate the guiding underlying master to guide the viral assembly, this process can be achieved via other low-cost techniques since the underlying surfaces act merely as guiding sacrificial scaffolds, which are subsequently removed. Methods such as imprinting or electrohydrodynamic lithography can be used to fabricate the guiding surfaces.<sup>[18]</sup> This facile technique provides the ability for a straightforward design, manufacture and control of highly reliable and robust submicron patterns at low cost, which can be utilized for the underlying guiding surfaces in the viral nanostructuring. Additionally, the guiding substrates can be made highly reusable by replicating the fabricated morphologies into a dimethylpolysiloxane/epoxy-based negative photoresist (PDMS/SU8) nanogratings coated by a metal nano-layer. Once the master is fabricated, it can be repeatedly used to produce the guiding substrates, making the viral nanopatterning even more cost-effective.

Given that the optical properties of nanometamaterials are closely related to the localized surface plasmon resonance (SPR) of the substrates, the ability to easily fabricate and tune propagating SPR properties and spectrum of metal nanostructures is highly attractive for developing new plasmonic devices.<sup>[19]</sup> Robust, scalable and easy fabrication methods of Fresnel lens structures are also of great technological interest due to their high focusing efficiency and ease of integration into optical components leading to the development of new compact focus sensors. Since the optical properties of nano-metamaterials differ from conventional optical materials, the concept of changing the shape and spacing of internal structures within a metamaterial opens the door to transforming light in many ways. Bulk optical metamaterials could further open prospects for studies of 3D optical effects and applications associated with them such as, the reverse Doppler effect, super lensing,

cloaking and camouflaging devices, optical tunneling devices, compact resonators and highly directional optical sources.

## 2. Results and Discussion

A range of concentric Fresnel lens-like nano-morphologies (Figure 1a–d) as well as micro- and nanogratings with varying ratios of ridge-to-groove (*R/G*) ranging from 0.18 to 1.0 (Figure 1e–h) were fabricated via focused ion beam (FIB) lithography and subsequently used as underlying guiding topographic surfaces for the fabrication of the various 3D nanoarchitectures from viral building blocks.

The micro-nanostructured surfaces were subsequently either immersed in the M13 solution (Figure 2a,b) or spin-coated (Figure 2c) in a controlled manner, followed by embedding the top in an epoxy/poly(methyl methacrylate) (PMMA) matrix and removal of the scaffold (Figure 2d), yielding three-dimensional free-standing bacteriophage-based assembled nano-morphologies. Quasi three-dimensional metal nanostructures were fabricated by plating with gold ( $2.1 \pm 0.9$  nm) via electrodeposition and sputtering. This yielded a range of topographic nanostructures, visible in the atomic force microscopy (AFM) height, polarized light microscopy (POM) and low-angle backscattered SEM images (Figure 3 and Figure S1, Supporting Information).

The use of topographically patterned substrates allows directing of the virus' orientation and specific pattern registration on a substrate, particularly appealing for applications requiring the addressability of nanoscale features. The fabricated physically heterogeneous surfaces with a range of *R/G* between 0.18 and 1.0 have been found to guide the self-assembly of the M13 phages in an interesting manner. While the topographic surfaces comprised of alternating ridges and

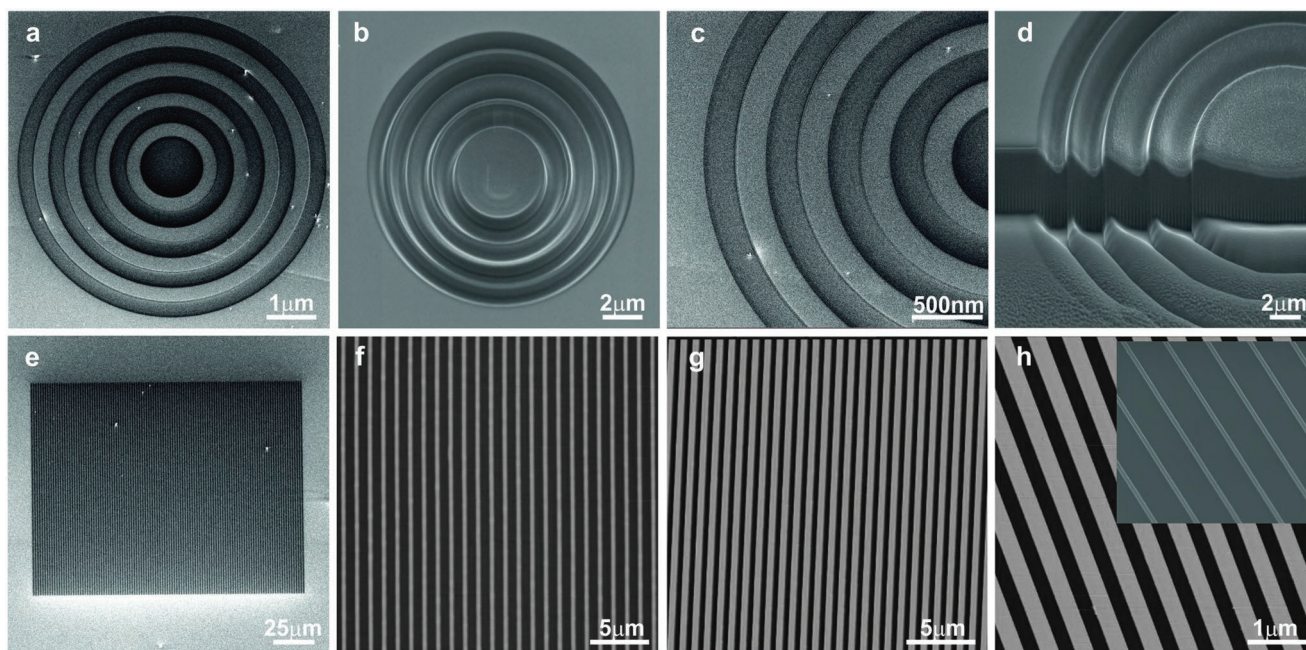


**Figure 1.** Representative scanning electron microscopy (SEM) images of the FIB fabricated underlying topological cues substrates of a–d) Fresnel-like nanotopologies, and of nanogratings with *R/G* ratios of e) 0.90, f) 0.54, g) 0.72, h) 0.75, and (inset) 0.18.



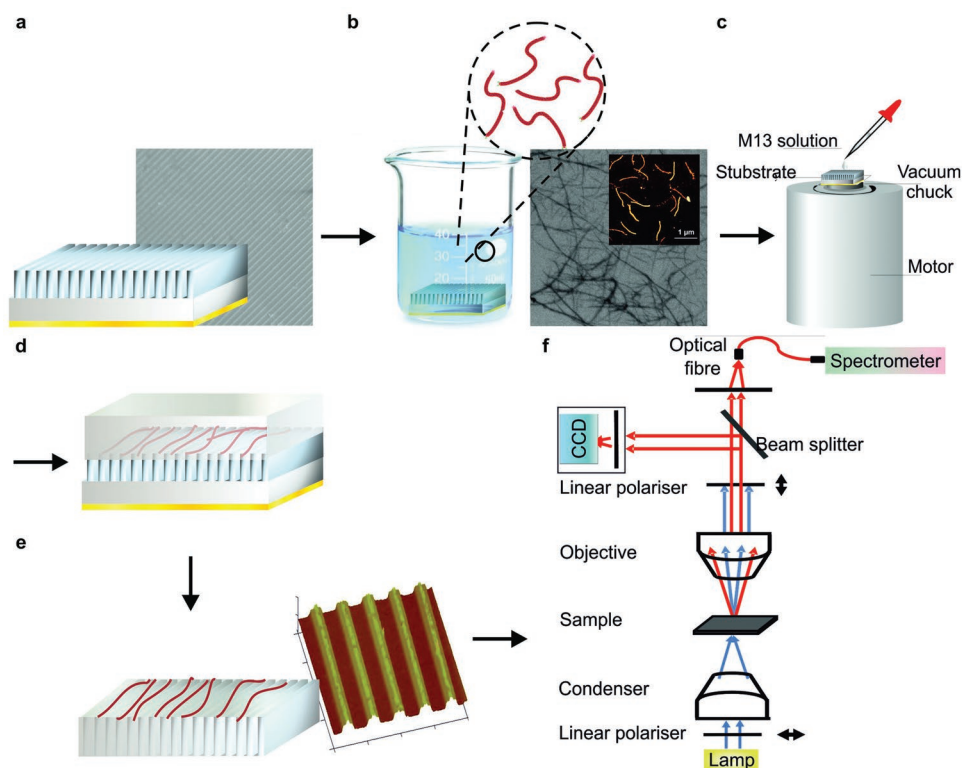


**Figure 2.** Schematics of the nanofabrication process to construct the three-dimensional nanometamaterials using self-assembling M13 building blocks as templates. a) Firstly, topographically micro and nanostructured surfaces were fabricated via FIB lithography to act as guiding underlying substrates for the M13. (inset) Representative SEM image of a silicon nanograting fabricated by FIB. Subsequently, substrates were either b) immersed in the M13 solution with dispersed bacteriophages shown in the corresponding SEM and AFM images (inset) or c) used for spin-coating the M13 solution. d) These were followed by embedding in epoxy/PMMA resin and e) release of the free-standing viral nanoarchitectures, which were then replicated into a metal *quasi* 3D nanostructure (inset) and f) the optical properties of gold-plated nanometaterials were characterized in terms of variations of the intensity of unpolarized and polarized light with attached spectrometer.

grooves guiding the M13 self-assembly via immersion-based deposition was found to induce a vertical alignment of the M13 (Figure 3a–d), the spin-coated periodic patterned surfaces directed the M13 to assemble perpendicular to the substrate, specifically registering with the underlying physical pattern in the middle areas of the underlying topographies (Figure 3e–h) and chiral liquid crystal nanostructures at the edges of the substrates (Figure 3i–l). For the vertical orientation of the M13 filaments, AFM image shows initially a small number of M13 phages aligning along the grooves (Figure 3a) followed by predominant vertical orientation after  $63 \pm 9$  min of immersion (Figure 3a, inset). The subsequent three-dimensional nonviral replicas, supported by the underlying epoxy/PMMA embedding (inverse to the original guiding surfaces) and plated with gold, are shown in Figure 3b,c with representative POM image of the LC phase in Figure 3d. SEM image in Figure 3e reveals the horizontal alignment of the M13 on the nanograting with  $R_H/G_H = 0.81$  with the free-standing replica (Figure 3f), perpendicularly oriented across the Fresnel-like nanolens structures (Figure 3g,h) and nematically ordered liquid crystal fiber bundles (Figure 3i–l).

The spatial resolution limit possible for our method is likely to be dictated by the viral dimensions. There is an interplay between the templating material (viral particles) and the larger-scale patterns constructed through fabrication. In all cases the

resolution required for the fabrication step of the large-scale structures can be lesser than that of the viral particle. We have used FIB to fabricate the larger scale trenches for viral assembly and given FIB's resolution down to  $\approx 5$  nm, this is highly suitable to achieve dimensions compatible with the viral particles which are 6.6 nm in diameter. Here we have chosen to fabricate the guiding surfaces with a resolution of  $\approx 20$  nm grooves and 50 nm ridges to enable sufficient self-assembly space for the viral strands to generate different optical behaviors, determined by the inter-virus arrangements within the assembled nano-morphologies. Thus overall, the fundamental limit of the fabrication method in our case is determined by the dimensions of the individual virus, which currently is 6.6 nm in diameter but will further depend on the choice of the templating virus.

To determine the average degree of anisotropy of the M13 filaments in vertical and horizontal orientations, SEM and AFM images were averaged over the entire structured area ( $\approx 1200 \mu\text{m} \times 1200 \mu\text{m}$ , 12 profiles). The maximum degree of vertical alignment was found for the grating with  $R_V/G_V = 0.39$  (Figure 4a) and of the horizontal alignment for  $R_H/G_H = 0.81$  (Figure 4b). For the horizontally oriented filaments, 83% of the M13 were aligned perpendicularly within  $\pm 21^\circ$  of the topographical feature direction and 63% were aligned vertically within  $\pm 18^\circ$  of the topographical cue director, in contrast to the

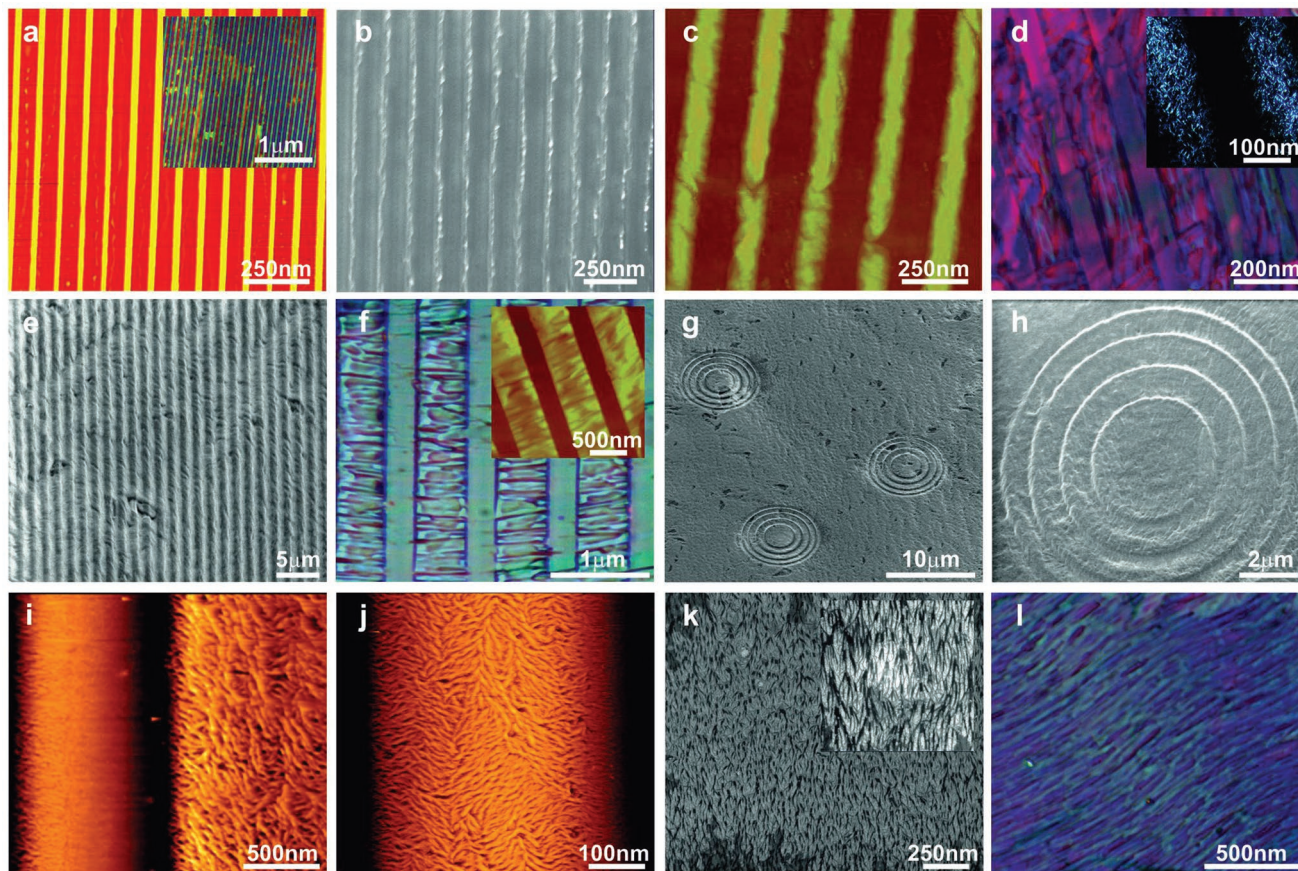


**Figure 3.** a) AFM and (inset) POM images of the longitudinal mode orientation of the M13 phages aligning along the length of the topological cue of the underlying nanograting. b) SEM, c) AFM, and d) POM images of the replicated viral nanograting morphologies. e) SEM image of the transverse mode orientation of the M13 bundles aligned horizontally across the underlying topographically structured substrate. Free-standing replicated horizontal viral morphologies of f) nanograting (inset: AFM height image) and g,h) Fresnel-like nanostructures. i,j) AFM height, k) SEM, and l) POM images of the replicated phage fiber bundle assembly in a groove and ridge areas yielding chiral liquid crystal nano-morphologies with nematicity twisted structures.

as-cast or immersion deposited films on planar substrate areas, where no preferred orientation was seen.

M13 nanofilms supported on patterned substrates exhibit a different behavior relative to the bulk due to ideal bulk configuration being hindered by the confinement of the M13 strands at the nano-interfaces. In the case of immersion in the M13 solution, there is an absence of confinement or chemical potential and initially the M13 assembly is somewhat a stochastic process, followed by the subsequent reduction of the free energy of the phage with the underlying physical cues, guiding the orientation of the M13 according to the balance of the interfacial energy due to the formation of interface and the nonlocal molecular repulsion. The underlying patterned surface of alternating grooves and ridges leads to the M13 phage alignment in parallel lines within the grooves. Though the initial M13 phages are randomly distributed, with time they diffuse into the grooves, reducing the overall system energy.

During the spin-coating, the phage is laterally confined, and it adjusts to the imposed boundary conditions. M13 in a confined geometry behaves differently from the ones in large volumes due to the dominance of the liquids surface and interfacial tension and surface forces at length scales below the capillary length. In this case, initially the substrate is being

wetted with the M13 solution and subsequently by rotating it at high speeds (700–3000 rpm), the centrifugal forces spread the solution to a nanolayer, with increasing angular spinning speeds resulting in a thinner distribution. While the supporting substrate is spinning at constant rotation rate, the viscous forces dominate the gradual and homogeneous thinning and orientation of the nano-layer and evaporation leads to a loss of solvent and an increase in the viscosity and density of the M13, slowing the shear thinning of the film. The competition between the centrifugal force and the evaporation rate is further controlled by the solution concentration, viscosity and rotation speed. These guide the assembly of the M13 phages on the underlying topographical surfaces. The perpendicular alignment is a result of the decrease in elastic energy in response to the confined arrangement formed by the spin-coating hybrid boundaries.<sup>[20]</sup>

Interestingly, in the periphery of the substrate, where the inherent “edge effect” of the spin-coating process is dominant, M13 phages organize into chiral LC nanostructures. In this pattern formation kinetics shear-thinning rate undulations appear in the thicker ridge region, with the Laplace pressure due to the surface tension smoothening the liquid distribution around the edge region complemented by the capillary



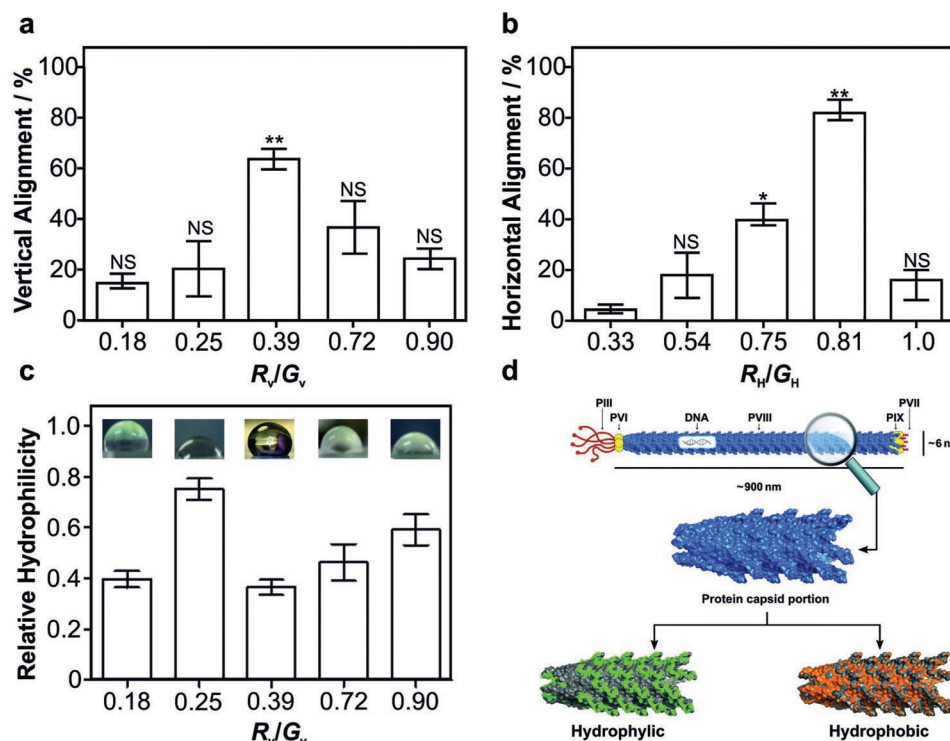


**Figure 4.** Degree of a) vertical and b) horizontal orientation for the various ridge to groove ratios of the underlying nanostructures. Percentage of the orientation is based on the deviation of the axis of the M13 longitude domains from the physical cue direction, with the difference between the critical wave vectors parallel and perpendicular to the cue direction changing with  $R_H/G_H$  or  $R_V/G_V$  ratios. A one-way ANOVA analysis shows a statistically significant difference in the  $R_V/G_V = 0.39$  and the  $R_H/G_H = 0.81$  ( $*p < 0.08$ ,  $**p < 0.05$ ). When degree alignment is zero, the morphology is isotropic. As the morphology becomes more oriented in the  $y$ -axis direction, which represents the critical wave vector along the direction parallel to domain alignment, becomes smaller, which in the case of perfect anisotropic alignment, will be 100%. c) Relative hydrophilicity as a function of the ridge-to-groove ratio for vertical orientations. d) Schematics of the 3D M13 virus, generated using 3D molecular visualization software PyMOL, with a section of the phage made of 35 copies of the PVIII assembled in the quaternary structure shown below (blue, PDB: 2MJZ).<sup>[23]</sup> The hydrophilic surface (green) corresponds to the amino acids of Arg, Lys, His, Glu, Asp, Asn, Gln, Thr, Ser, and Cys and the hydrophobic surface (orange) corresponds to Ala, Gly, Val, Ile, Leu, Phe, and Met.

flow caused by evaporation. The M13 fluid properties dictate a constant angle at the solid–liquid–gas interface and a thicker region is confined at the wafer edge. The spreading of a thin M13 bacteriophage film of liquid under the centrifugal force is comprised of a flat region, the dynamics of which is determined by the balance between driving forces and viscous dissipation and the edge region, governed by the interplay between the liquid surface tension and the driving evaporation force, increasing the concentration of the M13, in correspondence with the forming mechanism of chiral M13 film by Park et al.<sup>[21]</sup> The chiral LC nanopattern is driven by the increasing friction with air at the boundary, with the fluid in the center of the substrate, driven by centrifugal forces, flowing over the dry film, and building up at the edge.

For a Newtonian fluid M13 solution<sup>[22]</sup> with an absolute viscosity  $\eta$ , density  $\rho$  and velocity in the radial direction  $v$  with the radial coordinates  $r$ ,  $z$ , and  $\theta$  rotating with the plane at angular velocity  $\omega$  on a heterogenous, non-planar (i.e., topographically structured) surface the balance between centrifugal and viscous forces can be described by:

$$-\eta \left( \frac{d^2 \theta}{dz^2} \right) = \rho \omega^2 r \cos \theta - g \frac{r}{R_0} \quad (1)$$

where  $R_0$  is the ratio of the topographical cues of the substrate (grooves/ridges). In this regime the molecular order is controlled by the spinning time, speed, shear-thinning and the M13 bacteriophage film thickness:

$$h(r, t) = 1 / \left[ \frac{1}{h_0^2} + \frac{2t}{3R_0\eta} \left( -\frac{\rho\omega^2 r^2}{\sqrt{R_0^2 - r^2}} + 2\rho\omega^2 \sqrt{R_0^2 - r^2} - 2g \right) \right]^{0.5} \quad (2)$$

The orientation of the M13 nanofilms arises from a combination of the shear flow and elongational flow torque exerted on the M13 by the hydrodynamic convection forces and rotation by elongational component of the flow aligning the virus during pattern formation, probably minus the amount of orientation removed by relaxation and solidification at the surface. Based on Equations (1) and (2) the patterned underlying substrate guides the liquid flow more toward the center region if the spin speed is lower than 1200 rpm, and for the higher speeds the centrifugal force is increased sharply with less influence of the topological cues of the substrate on the uniformity of the M13 film. The chiral liquid crystal nanostructure at the edge of the topographically spin-coated substrate is a result of the interplay of kinetic factors including flux, LC transitions and elastic forces.<sup>[12]</sup>

We have subsequently studied the hydrophilicity and hydrophobicity properties of the fabricated nanostructures. Contact angle measurements on the fabricated viral nanostructures revealed that while the horizontally aligned viral morphologies did not impact the hydrophobicity of the final structures. In the case of the vertically assembled nanoarchitectures, there was a variation in the degree of hydrophilicity, with the viral grating of  $R_v/G_v = 0.39$  generating an apolar hydrophobic surface with a contact angle of  $130 \pm 12^\circ$  (Figure 4c). On the other hand, the rest of the  $R_v/G_v$  morphologies exhibited contact angles of a more hydrophilic nature except for the  $R_v/G_v = 0.18$ , with a contact angle of  $108 \pm 9^\circ$ .  $R_v/G_v = 0.39$  viral grating exhibited considerably increased water repellent properties due to the large surface contact area between the liquid droplet and the M13 protein capsid surface.

The surface of the M13 protein capsid is characterized by specific chemical and physical properties strictly related to the side chains of the more exposed amino acids. In solution, some of these residues can mediate electrostatic interactions at specific pH values, while other residues could play a role in hydrophobic interactions<sup>[4a]</sup> (Figure 4d). The wettability of the fabricated surfaces is not necessarily linked to the virus surface properties and might be due to the topology and the specific orientation of the M13 filaments on the substrates. In fact, once assembled, the virus is subjected to a series of templating sequences covering its surface, which therefore cannot interact directly with the deposited drop during the contact angle measurements. Therefore, while the chemical and physical surface

properties of M13 and the forces to which the viral particles are subject are crucial during the assembly process, the properties of templating gold combined with the nanoroughness of the obtained surface define the wettability of these nanostructured materials. In a densely packed porous network of the M13-roughness with *minute* variations in heights, upon wetting with a water drop, a thin layer of liquid is left behind and the solid fraction in contact with liquid is increased with the network being penetrated by water, yielding the high solid-water adhesion and therefore, contact angle hysteresis. On the other hand, closely packed M13 nanostructure restrains the droplet spread, leading to a larger contact angle and a roll-off hydrophobicity. However, the surface nanoroughness must still be maintained, because a too dense structure will gradually result in a closure of the porous network, decreasing the water repellence.<sup>[24]</sup> Moreover, since the surface roughness of the M13 fiber bundles can be controlled, it might be possible to further tune the degree of the apolar properties for the replicated structures.

Interesting optical properties, different to bulk gold, emerge in the fabricated metamaterial-like viral nanostructures. Reflectance spectra in the visible range on each gold-plated nanostructure sample are shown in Figure 5a. A distinct change in the position of the extinction wavelength maximum is seen for the gold infiltrated viral nano-morphologies. The primary extinction peak for the chiral nematic liquid crystal nanostructure is observed around 485 nm in reflection mode, with the wavelength maximum red-shifting progressively yielding broader peaks for the vertically oriented (longitudinal

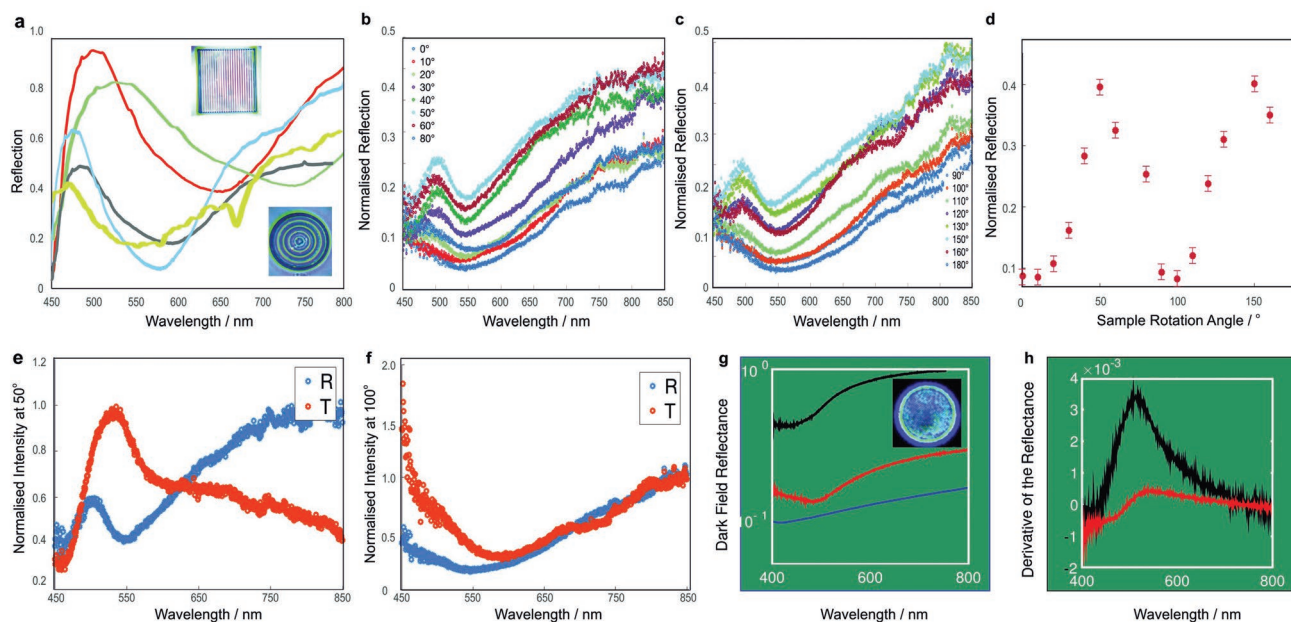


**Figure 5.** a) Reflection spectra for unpolarized incident light of chiral liquid crystal nanostructure (blue), vertically oriented viral ridges (red), horizontally aligned grating nanostructures (green), dielectric (black), and metallic Fresnel-like nanoviral morphologies (yellow). Reflectance spectra of the vertically oriented viral ridges from the polarized illumination ( $0^\circ$  indicating the position where the sample is parallel to the polarization of the incoming light, reference: mirror, parallel polarizers) while rotating the sample between b)  $0^\circ$  and  $80^\circ$ , and c)  $90^\circ$  and  $180^\circ$  angles. d) Variation in reflection extinction peak position and width as a function of the sample angle. Normalized reflection ( $R$ , blue) and transmission ( $T$ , red) intensity spectra of the vertically oriented viral nanogratings at their e) maximum and f) minimum positions, normalized to values at  $800\text{ nm}$ , a  $50^\circ$  and  $100^\circ$ , respectively. g) Dark field reflectance spectra of the (blue) as-fabricated viral with no gold, (black) pure gold, nanolayer with the same deposition parameters, and (red) gold reproduced horizontal grating nanostructures. h) Plasma-edge, the spectral position of the maximum of the derivative reflectance of horizontal grating nanostructures (red) relative to pure gold nanolayer (black).

mode, along the length) viral ridges at 500 and 525 nm for the horizontally aligned (transverse mode) grating-like nanostructures.<sup>[12,25]</sup> While an Au surface plasmon can be shifted to 500 nm or below, similar extinction at 520 nm has been observed for 10 nm nanoparticles and in this case is due to the modification of the plasma frequency by the nano-structuring and corresponding air fraction.<sup>[26]</sup> This is in agreement with the nanorod-like structure at normal incidence, with the short-wavelength transverse mode of the rods matching that of 10 nm gold nanoparticles and the long-wavelength longitudinal mode produced by the optical field along the rod-like structure as shown by Vignolini et al.<sup>[27]</sup>

Reflectance spectra are known to depend on the structural motifs, e.g., size of the nano-moieties, pitch and dielectric filling.<sup>[28]</sup>

Also, the polarization of domains with respect to the incident light can yield similar spectral blue shift of metamaterials.<sup>[27]</sup> For the Fresnel-like nanoviral morphologies the reflectance is red shifted, producing unusual optical properties caused by a symmetric geometric reflection off the sides of each circular ridge. Comparing the reflectance spectra of these non-coated viral structures (dielectric) and the gold-plated periodically modulated surfaces (metallic), characteristic extinction peaks are found at 490 and 470 nm, accordingly with the latter exhibiting additional absorption dips arising from the resonant coupling to surface plasmon polaritons enabled by the metallic nanostructures. Light polarized in different directions couples differently to localized plasmon resonances of the gold nanonetwork.<sup>[27]</sup>

Normalized reflectance spectra measured from the polarized illumination (measuring the total incident light) while rotating the vertically oriented viral ridges sample between 0° and 180° angles reveal a characteristic extinction peak at around 500 nm for all samples (Figure 5b,c). On rotating the sample, the polarization angle of incidence changes by twice the amount, which explains that the spectrum at 90° is nearly identical to that at 0°. A periodicity of 90° in the peak intensity (Figure 5d) is thus to be expected. However, no periodicity is observed for any of the other peaks indicating that the regularity of the plasmonic nanostructure as the underlying cause of this absorption of the peak at ≈500 nm. The other features are very likely the result of interactions between the plasmons excited within the metamaterial at specific polarizations. The same periodicity is present both for the maximum and the minimum peak intensities. Figure 5e,f shows a comparison of transmission and reflection spectra at their maximum (≈50°) and minimum (90°) positions with the spectra normalized relative to values at 800 nm. An increasing absorption at shorter wavelengths is seen in these reflection spectra with a peak tuning sinusoidally with the polarization direction with the spectral linewidth of the band being of the latter. Interestingly the reflectance extinction (Figure 5e) at the position where the observed polarization minimum (Figure 5d) is significant, almost 0.1, indicating a high degree of alignment in the orientation of the phages. Moreover, this confirms that their orientation is orthogonal to the direction of the sample (as apparent in Figure 3) and the distribution is highly anisotropic. While we see a peak at 485 nm, we also see a drop in intensity at 550 nm. This peak and the dip are polarization dependent, which is to be expected in anisotropic

(periodically varying refractive index) plasmonic materials that will result in anisotropic resonances. The increased absorption or non-reflection can arise likely due to destructive interference as a result of phase shifts of the reflected wave from different parts of the nanostructure similar to that seen in nanograting architectures.<sup>[29]</sup> Dark field spectra of the transverse mode perpendicularly organized viral nanostructures (acquisition with fiber = 100 μm, 50×) with the gold layer of the same thickness acting as a reference. This nanostructure shows a red shift in the plasma edge, i.e., the spectral position of the maximum of the derivative of around 25 nm compared to the pure gold nanolayer, being similar to what has been measured and predicted for gyroids and other “porous gold” metamaterials.<sup>[25,27,30]</sup> For single gyroid metamaterials fabricated in gold, properties such as enhanced transmission have been previously observed due to their sub-wavelength architectures and the arising plasmon resonances.<sup>[30]</sup>

To note that the localized surface plasmon resonance of the substrates and the optical properties are related and the optical properties of nanometamaterials, even though fabricated from plasmonic materials, are dominated by those due to their intrinsic structure and most importantly the fill-fraction. Plasmon length scales are of the order of ≈100 nm, indicating that plasmons are excited in these new nanometamaterials. The reflectance dips in Figure 5, shifting to higher wavelengths, with high extinction between 550 and 650 nm and the broadened peaks are due to the localized surface plasmon resonances and their hybridization. The shifts relate to the metamaterial nature while the broadening indicates interactions between the plasmons. The polarization properties are unique due to the choice of anisotropic biosynthetic materials used to produce the structure. Overall, the reflectance spectra of these structures indicate that the optical properties are more than only due to plasmonic absorption, indicating that further understanding of nanometamaterials and their optical properties is going to be an area of active and ongoing research.

### 3. Conclusions

A new *bottom-up* guided viral M13 nano-assembly technique has been established for advanced, straightforward *quasi* three-dimensional fabrication of nanostructured metamaterials. This proof-of-concept method for artificially engineered nanomaterials can give rise to unique and intriguing properties, which are not available in nature, including optical metamaterials with unprecedented photonic properties.

A range of nano-configurations were produced via varying underlying topologically structured substrates, which directed the M13 self-assembly, yielding vertically aligned and horizontally oriented nanoviral gratings, Fresnel-like nanoarchitectures and chiral liquid-crystal like nano-morphologies. Subsequently, surface energy and optical properties were studied for the newly fabricated nanomaterials. Several of the generated nanoviral structures enable enhancing the hydrophobicity via different length scales of roughness and the specific orientation of the M13 filaments on the substrates with the closely packed phage nanostructure restraining the droplet spread, resulting in a larger contact angle and a roll-off hydrophobicity.



The plasmonic viral metallic grating with nanometer periods at the substrate layer yields enhanced reflection, with a confinement induced energy arising from plasmons localized in the gold viral concentric rings of the Fresnel-like nanostructures. Ordered nanometer-scale viral networks further resulted in the modification and shift of the plasma frequency yielding metamaterials with distinct optical characteristics different from bulk gold and with modes similar to that observed by Vignolini et al.<sup>[27]</sup> The fabricated gold-viral nanograting like structure exhibits high reflection (>90%) in the visible range and (>50%) over a broad range of wavelengths from visible to near-infrared. The chiral LC nanostructure exhibit a medium reflection (60%) and a lower reflection (>40%) is found for the Fresnel-like viral-Au nanoarchitectures over the same range of wavelengths.

Scale-up approaches for the established method might include one or a combination of several processes, such as continuous roll-to-roll top-down/bottom-up or parallel large-area processes, semi-continuous or continuous either chemical, fluid or thermal techniques for biomolecular nanofabrication. The overall process will typically be carried out in three consecutive stages in which the nanostructure production is scaled up by an order of magnitude each time. Considering a larger scale fabrication for our technique, large scale spin-coating processes already exists and mass production of the viral building blocks of the M13 is also feasible. Traditionally, M13 is propagated in bulk via infecting a culture of *Escherichia coli*. After the propagation, M13 is purified via polyethylene glycol/sodium chloride (PEG/NaCl) precipitation with approximately a 6 L culture being sufficient to produce 100–500 mg of M13. This is a quick (48 h) and simple process generally employed in the lab.<sup>[6,31]</sup> The propagation of M13 can be easily scaled up employing larger culture volumes and fermenters.<sup>[32]</sup> Also employing purification methods such as aqueous two-phase systems, which are more convenient for the large-scale production of M13.<sup>[33]</sup>

In the long-term this method will lay a platform for developing the ability to design and fabricate new artificial nanostructures to create photonic metamaterials and thus, be a herald of a substantial advance in the manufacture of essential three-dimensional nanostructured ingredients, which can be employed in the development of advanced photonic nano-devices. As such, it has the potential to address some of the more intractable problems facing the defense and security sectors and open new avenues in protecting the armed forces and civilian populations. It will have many applications through metamaterials that have low observable properties in the visible or infrared ranges, important for the survivability of people and equipment, and on to nano-lenses that enable imaging with sub-wavelength resolution, or optical concealing devices, which provide invisibility for macroscopic objects. Low-density nanostructured metamaterials could also lead to lightweight miniature devices and systems at the same time with enhanced performance. The generated superhydrophobic nanoviral surfaces are further promising prospects for both the fundamental research of nanoscale scale hydrophobicity and broader applications including, microfluidics, energy harvesting<sup>[14c,34]</sup> and sensors.<sup>[35]</sup> A new technique constructing metamaterials using self-assembling M13 viral building-blocks, therefore, could open a new avenue for the generation of a broad

spectrum of high-fidelity alternating hydrophobic/hydrophilic patterns in a straightforward and low-cost fashion, requiring no vacuum processing, no hazardous organic compounds with possibilities of exploiting original synthetic biology, rendering this technique even more technologically appealing.

## 4. Experimental Section

**Focused Ion Beam Lithography:** Focused ion beam Lithography (FIB) was used to produce the micro- and nano-structured underlying surfaces. Highly polished p-doped silicon (Si) wafers, with <100> crystal orientation (Wafernet GmbH, Eching, Germany) covered by a 100 nm thick silicon oxide layer were used as substrates. Transparent indium-tin oxide (ITO) covered glass slides with a resistivity of 80 Ω cm<sup>-2</sup> were also used, allowing in situ optical tracking. Initially, the substrates were cleaned in a “Piranha” solution consisting of 3:1 H<sub>2</sub>SO<sub>4</sub> (98%):H<sub>2</sub>O<sub>2</sub> (30%), followed by thorough rinsing with deionized water and dried under N<sub>2</sub>. Subsequently, silicon wafers and ITO were cleaned using a snow-jet gun immediately before the FIB process. Dual beam scanning microscope, FEI Helios 200D, with a scanning focused ion beam at an angle of 52° and a vertical imaging electron beam was used to fabricate the desired patterns. To generate the gratings, positive gallium ions were focused using electrostatic lenses form a spot on the surface of the sample. A sharp tungsten needle with a spiral container of gallium mounted on the back pointing downward was heated to melt the gallium which due to gravity and capillary forces coated the tungsten needle. A high electric field (2–4 kV) between the needle and a cathode formed a sharp liquid tip. The high electric field released gallium ions from the sharp tip, which were then accelerated toward the cathode. Gallium ions were subsequently focused and accelerated using a series of electrostatic octopole and hexapole lenses to a spot on the sample. The ion beam was accelerated between 500 V and 30 kV. The beam of gallium ions was moved over the target surface, creating the desired patterns via a built-in lithography system, i.e., FEI Nanobuilder. To fabricate the Fresnel lenses, a single crystal silicon substrate was used with an ion beam accelerated at 30 kV. Different dwell times were used to create a range of depths and shapes of sputter and the sloped sides of the lenses.

**M13 Solution:** M13 bacteriophage (M13KE) (New England Biolabs) double-stranded DNA was transferred into One Shot TOP10F' Chemically Competent *E. coli* (Thermo Fisher Scientific) through a heat shock. Subsequently, it was self-propagated in batch cultures using the *E. coli* strain. The process includes, 2 L of Nutrient Broth No. 2 (Thermo Fisher Scientific Oxoid) autoclaving, to which, once cooled down to room temperature, tetracycline was added to a final concentration of 5 µg mL<sup>-1</sup>. Then, M13 and *E. coli* were inoculated and incubated at 37 °C, 150 rpm for 24 h. After the propagation, the culture was centrifuged twice at 8000 rpm (Beckman Coulter JA 10, RCF = 11 295.1g) and the pellet containing the *E. coli* was discarded. The supernatant containing M13 was subsequently incubated with PEG 6000 (Sigma-Aldrich) and stirred for 90 min at 4 °C. Finally, the supernatant/PEG solution was centrifuged at 10 000 rpm (Beckman Coulter JA 10, RCF = 17 648.6g). The supernatant was then discarded. The obtained white pellet was resuspended in DIW and the pH of the solution was brought to pH = 4, provoking the flocculation of M13. The flocculated sample was split into microtubes and centrifuged for 5 min at 15 000 rpm (SciSpin MICRO, SciQuip, RCF = 15 100g) and the supernatant was discarded. The resultant white pellet of M13 was resuspended in DIW and centrifuged again (5 min at 15 000 rpm) to remove any insoluble fraction. The M13 concentration of (typically, 3–9 mg mL<sup>-1</sup>) was determined with a UV-vis spectrophotometer (CaryWin-UV, Agilent Technologies), measuring the absorbance at 269 nm.<sup>[6]</sup>

**Nano-Substrates Preparation:** To obtain the equilibrium self-assembled surface morphologies, the M13 nanofilm was prepared via immersion of the structured surfaces in the M13 solution (15–90 min, DIW from PBS pH 7.4), followed by drying under a constant N<sub>2</sub> flow and/or spin-coating of the M13 solution on the structured

surfaces (Laurell VWS-400B-6NPPLTE). The substrate was typically accelerated for the dynamic dispense at 700 rpm with various spin acceleration times ( $t_{Acc} = 10\text{--}30$  s) following by the spin casting at the final spin speed of 1000–3000 rpm for 30–60 s. The humidity in the chamber was controlled via a constant dry  $N_2$  gas flow and controlled spinning time, speed, acceleration, and the deposition shearing rates. To minimize contaminations, the spin-coating procedure was performed in clean-room conditions. Subsequent to the M13 deposition on the patterned surfaces, the overall self-assembled sample was embedded in a Spurr epoxy resin at 60 °C for 2 h or in a poly (methyl methacrylate) (PMMA), where a homogeneous PMMA layer was spin-cast on a silicon wafer, followed by placing the patterned Si/ITO-M13 on top (i.e., facing the PMMA film) and annealing at 45 °C for 1 min. The sample was allowed to cool to RT, resulting in a solidification of the film while embedding the upper end of the M13 nanomorphology, which was subsequently peeled off the underlying patterned surfaces. The resulting nanostructures were gold-plated via electrodeposition with an initial nucleation step of 0.0 and  $-1.2$  V and a  $50$  mV  $s^{-1}$  at scan rate followed by the deposition step (3 s,  $-0.8$  V) up to a thickness in the range between 2 and 3 nm.<sup>[36]</sup> The nanostructures were alternatively coated with a thin gold nanofilm using an Emitech sputter-coater with a direct current argon plasma (Au of 99.999% purity, Kurt J. Lesker) using two cycles of 10 s at 70 mA.

**Contact Angle Measurements:** Contact angle was measured using a computer controlled telescopic goniometer (KSV CAM 200) with digital image acquisition. A numerical fitting algorithm was applied to determine the advancing and receding contact angles from the side-view of the drops. Static contact angles were measured on drops and the images were fitted using the contact angle goniometer software. A Young–Laplace fitting algorithm was used, and a base-line tilt was allowed. The images of the advancing and receding drops were analyzed using ImageJ (Drop Analysis Package).

**Optical Characterization:** A Leica DM2000 optical polarizing microscope was used to investigate the optical properties of the samples. The optical transmission and reflection characterization of the samples was evaluated in terms of variations of the intensity of light using unpolarized incident light and the attached spectrometer (Horiba). The microscope Xenon lamp acted as an illumination source for the spectroscopic measurements. 20–100  $\mu$ m optical fibers (ThorLabs) in the focal plane of the 20 $\times$  objective working distance has served as a pinhole for the signal collection. Motorized MicroHR Imaging Spectrometer with a solid-state UV coated silicon over indium gallium arsenide detector for 200–1700 nm and the SynerJY for Windows software were used for data acquisition and analysis. Achromatic polarizers (Thorlabs) were used for polarization measurements. For transmission and reflection measurements in different directions, the sample was mounted on a multirotational stage enabling both the rotation around the focal axis of the objective and tilting away from normal incidence.

**Scanning Electron Microscopy:** Scanning Electron Microscopy (SEM) characterization was performed using a LEO ULTRA 55 SEM including a Schottky emitter (ZrO/W cathode) as well as a thermally assisted field emission source scanning electron microscope (FEI Helios dual beam) at acceleration voltages of 1–10 kV with a lateral resolution of 2–5 nm.

**Atomic Force Microscopy:** JPK NanoWizard II atomic force microscope was used to characterize the surfaces' topography. The atomic force microscopy (AFM) measurements were performed using tapping mode via an intermittent contact of the tip with the sample in ambient conditions. NCHV-A cantilevers with a resonance frequency of 320 kHz and stiffness of 42  $Nm^{-1}$  were used. Height and phase images were analyzed with Gwyddion's software (Version 2.55). Each scan was performed at 1024  $\times$  1024 pixel quality at 3 s per line raster rate, for a total of 1 h per region.

## Supporting Information

Supporting Information is available from the Wiley Online Library or from the author.

## Acknowledgements

The authors acknowledge funding from the Wellcome Trust (1741SSFPF), the Royal Academy of Engineering (RF1415\14\28), the Defence Science and Technology Laboratories (DSTLX-1000098511), BAE Systems (1464085), and the EPSRC. P.G.O. is a Royal Academy of Engineering Research (RAEng) Fellowship holder.

## Conflict of Interest

The authors declare no conflict of interest.

## Data Availability Statement

The data that support the findings of this study are available from the corresponding author upon reasonable request.

## Keywords

M13 viral building-blocks, nanometamaterials, optical properties

Received: December 21, 2021

Revised: April 11, 2022

Published online:

- [1] a) N. V. Dung, B. S. Tung, B. X. Khuyen, Y. J. Yoo, Y. Lee, J. Y. Rhee, V. D. Lam, *J. Korean Phys. Soc.* **2016**, *68*, 1008; b) T. F. Krauss, R. M. De La Rue, *Prog. Quantum Electron.* **1999**, *23*, 51; c) H. Tao, N. I. Landy, C. M. Bingham, X. Zhang, R. D. Averitt, W. J. Padilla, *Opt. Express* **2008**, *16*, 7181.
- [2] a) Z. Li, Z. Ge, X.-Y. Zhang, Z.-Y. Hu, D. Zhao, J.-W. Wu, *Indian J. Phys.* **2019**, *93*, 511; b) A. Pandey, S. B. Rana, *Res. Cell. Int. J. Eng. Sci.* **2016**, *17*, 359; c) C. M. Soukoulis, *Photoniques* **2018**, *1*, 50; d) I. Nefedov, S. Tretyakov, *Phys. Rev. E: Stat., Nonlinear, Soft Matter Phys.* **2002**, *66*, 036611; e) N. Engheta, R. W. Ziolkowski, *Metamaterials: Physics and Engineering Explorations*, John Wiley & Sons, Hoboken **2006**; f) J. Li, L. Zhou, C. T. Chan, P. Sheng, *Phys. Rev. Lett.* **2003**, *90*, 083901; g) M. Johri, Y. A. Ahmed, T. Bezboruah, *Curr. Sci.* **2007**, *92*, 1361.
- [3] a) P. S. Chinthamanipeta, Q. Lou, D. A. Shipp, *ACS Nano* **2011**, *5*, 450; b) E. J. W. Crossland, M. Kamperman, M. Nedelcu, C. Ducati, U. Wiesner, D. M. Smilgies, G. E. S. Toombes, M. A. Hillmyer, S. Ludwigs, U. Steiner, H. J. Snaith, *Nano Lett.* **2009**, *9*, 2807.
- [4] a) P. Passaretti, Y. Sun, T. R. Dafforn, P. G. Oppenheimer, *RSC Adv.* **2020**, *10*, 25385; b) V. A. Petrenko, *Viruses* **2018**, *10*, 311.
- [5] a) J. H. Lee, C. M. Warner, H. E. Jin, E. Barnes, A. R. Poda, E. J. Perkins, S. W. Lee, *Nat. Protoc.* **2017**, *12*, 1999; b) S. W. Lee, C. Mao, C. E. Flynn, A. M. Belcher, *Science* **2002**, *296*, 892.
- [6] P. Passaretti, I. Khan, T. R. Dafforn, P. G. Oppenheimer, *Sci. Rep.* **2020**, *10*, 18538.
- [7] W. O. Salivar, H. Tzagoloff, D. Pratt, *Virology* **1964**, *24*, 359.
- [8] P. Moghimian, S. V. Pichon, B. Facey, S. Aken, P. J. Biomater. Nanobiotechnol. **2016**, *7*, 72.
- [9] K. Mohan, G. A. Weiss, *ACS Chem. Biol.* **2016**, *11*, 1167.
- [10] a) J. M. L. Bernard, M. B. Francis, *Front. Microbiol.* **2014**, *5*, 734; b) N.-M. D. Courchesne, M. T. Klug, P.-Y. Chen, S. E. Kooi, D. S. Yun, N. Hong, N. X. Fang, A. M. Belcher, P. T. Hammond, *Adv. Mater.* **2014**, *26*, 3398.
- [11] a) P. Passaretti, Y. Sun, I. Khan, K. Chan, R. Sabo, H. White, T. R. Dafforn, P. G. Oppenheimer, *Nanoscale* **2019**, *11*, 13318;

- b) Y. Sun, P. Passaretti, I. Hernandez, J. Gonzalez, W. Liu, F. Rodriguez, D. J. Dunstan, P. Goldberg Oppenheimer, C. J. Humphreys, *Sci. Rep.* **2020**, *10*, 15618; c) M. Tridgett, L. Lozano, P. Passaretti, N. R. Desai, T. J. Proctor, H. A. Little, R. T. Logan, K. P. Arkill, P. G. Oppenheimer, T. R. Dafforn, *Bioconjugate Chem.* **2018**, *29*, 3705.
- [12] W.-J. Chung, J.-W. Oh, K. Kwak, B. Y. Lee, J. Meyer, E. Wang, A. Hexemer, S.-W. Lee, *Nature* **2011**, *478*, 364.
- [13] S. Zhang, H. Yu, J. Yang, Z. Shen, *Environ. Sci.: Nano* **2017**, *4*, 876.
- [14] a) D. Kim, M. Gu, M. Park, T. Kim, B.-S. Kim, *Mol. Syst. Des. Eng.* **2019**, *4*, 65; b) J. H. Lee, J. H. Lee, J. Xiao, M. S. Desai, X. Zhang, S. W. Lee, *Nano Lett.* **2019**, *19*, 2661; c) I. W. Park, K. W. Kim, Y. Hong, H. J. Yoon, Y. Lee, D. Gwak, K. Heo, *Nanomaterials* **2020**, *10*, 567.
- [15] C. Li, J. Li, Y. Xu, Y. Zhan, Y. Li, T. Song, J. Zheng, H. Yang, *Int. J. Pept. Res. Ther.* **2020**, *1*.
- [16] J. Paczesny, K. Bielec, *Nanomaterials* **2020**, *10*, 1944.
- [17] Y. Ma, R. J. Nolte, J. J. Cornelissen, *Adv. Drug Delivery Rev.* **2012**, *64*, 811.
- [18] a) P. G. Oppenheimer, *Electrohydrodynamic Patterning of Functional Materials*, Springer, Heidelberg **2013**; b) P. Goldberg-Oppenheimer, P. Kohn, R. M. Langford, U. Steiner, *Small* **2012**, *8*, 2595; c) P. Goldberg-Oppenheimer, U. Steiner, *Small* **2010**, *6*, 1248.
- [19] a) L. A. Obando, K. S. Booksh, *Anal. Chem.* **1999**, *71*, 5116; b) A. Baba, J. Lübben, K. Tamada, W. Knoll, *Langmuir* **2003**, *19*, 9058; c) A. Baba, K. Tada, R. Janmanee, S. Sriwichai, K. Shinbo, K. Kato, F. Kaneko, S. Phanichphant, *Adv. Funct. Mater.* **2012**, *22*, 4383; d) V. Stockhausen, P. Martin, J. Ghilane, Y. Leroux, H. Randriamahazaka, J. Grand, N. Felidj, J. C. Lacroix, *JACS* **2010**, *132*, 10224; e) A. Yoshida, K. Imazu, X. Li, K. Okamoto, K. Tamada, *Langmuir* **2012**, *28*, 17153.
- [20] Y. Yan, P. Zhou, S.-X. Zhang, X.-G. Guo, D.-M. Guo, *Chin. Phys. B* **2018**, *27*, 068104.
- [21] S. M. Park, W.-G. Kim, J. Kim, E.-J. Choi, H. Kim, J.-W. Oh, D. K. Yoon, *Small* **2021**, *17*, 2008097.
- [22] M. T. Gallagher, C. V. Neal, K. P. Arkill, D. J. Smith, *J. R. Soc., Interface* **2017**, *14*, 20170564.
- [23] O. Morag, N. G. Sgourakis, D. Baker, A. Goldbourn, *Proc. Natl. Acad. Sci. U. S. A.* **2015**, *112*, 971.
- [24] a) P. Xu, J. R. Bai, P. Zhou, L. L. Wang, X. N. Sun, L. Wei, Q. F. Zhou, *RSC Adv.* **2022**, *12*, 2701; b) A. Misiura, C. Dutta, W. Leung, J. Zepeda O, T. Terlier, C. F. Landes, *J. Chem. Phys.* **2022**, *156*, 094707; c) J. Macko, N. Podrojková, R. Oriňaková, A. Oriňak, *Nanomater. Nanotechnol.* **2022**, <https://doi.org/10.1177/18479804211062316>; d) A. Bayat, M. Ebrahimi, A. Z. Moshfegh, *Vacuum* **2014**, *101*, 279.
- [25] C. Banbury, J. J. S. Rickard, S. Mahajan, P. G. Oppenheimer, *ACS Appl. Mater. Interfaces* **2019**, *11*, 14437.
- [26] J. A. Dolan, M. Saba, R. Dehmel, I. Gunkel, Y. Gu, U. Wiesner, O. Hess, T. D. Wilkinson, J. J. Baumberg, U. Steiner, B. D. Wilts, *ACS Photonics* **2016**, *3*, 1888.
- [27] S. Vignolini, N. A. Yufa, P. S. Cunha, S. Guldin, I. Rushkin, M. Stefik, K. Hur, U. Wiesner, J. J. Baumberg, U. Steiner, *Adv. Mater.* **2012**, *24*, OP23.
- [28] P. Farah, A. Demetriadou, S. Salvatore, S. Vignolini, M. Stefik, U. Wiesner, O. Hess, U. Steiner, V. K. Valev, J. J. Baumberg, *Phys. Rev. Appl.* **2014**, *2*, 044002.
- [29] S. Li, M. Panmai, S. Tie, Y. Xu, J. Xiang, S. Lan, *Nanophotonics* **2021**, *10*, 1553.
- [30] S. Salvatore, A. Demetriadou, S. Vignolini, S. S. Oh, S. Wuestner, N. A. Yufa, M. Stefik, U. Wiesner, J. J. Baumberg, O. Hess, U. Steiner, *Adv. Mater.* **2013**, *25*, 2713.
- [31] K. Jurač, D. Nabergoj, A. Podgornik, *Appl. Microbiol. Biotechnol.* **2019**, *103*, 685.
- [32] a) B. Kick, S. Hensler, F. Praetorius, H. Dietz, D. Weuster-Botz, *Biotechnol. Bioeng.* **2017**, *114*, 777; b) B. Kick, F. Praetorius, H. Dietz, D. Weuster-Botz, *Nano Lett.* **2015**, *15*, 4672; c) R. García, S. Latz, J. Romero, G. Higuera, K. García, R. Bastías, *Front. Microbiol.* **2019**, <https://doi.org/10.3389/fmicb.2019.01187>; d) K. Machida, H. Imataka, *Biotechnol. Lett.* **2015**, *37*, 753.
- [33] M. Torres-Acosta, A. González-Mora, F. Ruiz-Ruiz, M. Rito-Palomares, J. Benavides, *J. Chem. Technol. Biotechnol.* **2020**, *95*, 2822.
- [34] H. Kim, J.-H. Lee, J. H. Lee, B. Y. Lee, B. D. Lee, K. Okada, S. Ji, J. Yoon, J. H. Lee, S.-W. Lee, *Nano Lett.* **2021**, *21*, 6851.
- [35] J.-S. Moon, E. J. Choi, N.-N. Jeong, J.-R. Sohn, D.-W. Han, J.-W. Oh, *Nanomaterials* **2019**, *9*, 1448.
- [36] R. E. Tucker, *Universal Metal Finishing Guidebook*, Elsevier, Congers, NY **2012**.